

Cross-Modal Geometric Hierarchy Fusion: An Implicit-Submap Driven Framework for Resilient 3D Place Recognition

Xiaohui Jiang, Haijiang Zhu, Chadei Li, Fulin Tang, and Ning An

Abstract—LiDAR-based place recognition serves as a crucial enabler for long-term autonomy in robotics and autonomous driving systems. Yet, prevailing methodologies relying on hand-crafted feature extraction face dual challenges: (1) Inconsistent point cloud density, induced by ego-motion dynamics and environmental disturbances during repeated traversals, leads to descriptor instability, and (2) Representation fragility stems from reliance on single-level geometric abstractions that lack discriminative power in structurally complex scenarios. To address these limitations, we propose a novel framework that redefines 3D place recognition through density-agnostic geometric reasoning. Specifically, we introduce an implicit 3D representation based on elastic points, which is immune to the interference of original scene point cloud density and achieves the characteristic of uniform distribution. Subsequently, we derive the occupancy grid and normal vector information of the scene from this implicit representation. Finally, with the aid of these two types of information, we obtain descriptors that fuse geometric information from both bird’s-eye view (capturing macro-level spatial layouts) and 3D segment (encoding micro-scale surface geometries) perspectives. We conducted extensive experiments on numerous datasets (KITTI, KITTI-360, MulRan, NCLT) across diverse environments. The experimental results demonstrate that our method achieves state-of-the-art performance. Moreover, our approach strikes an optimal balance between accuracy, runtime, and memory optimization for historical maps, showcasing excellent Resilient and scalability. Our code will be open-sourced in the future.

Index Terms—LiDAR, place recognition, Implicit Neural Representation, 3D descriptors

I. INTRODUCTION

PLACE recognition, the capability of identifying previously visited locations in unmanned systems, serves as a cornerstone for achieving long-term autonomy in robotics and self-driving platforms [1]. This capability is crucial for autonomous mobile robots to achieve precise and robust positioning in unknown environments [2]. Place recognition also has a wide range of applications. For instance, it is used in loop closure detection for Simultaneous Localization and Mapping (SLAM) [3]–[5], map merging in large-scale scene mapping [6], and autonomous robot navigation [7], [8]. Light

This work was supported in part by the National Natural Science Foundation of China (Grant No.62202468 and No. 92367111) and the Key Science and Technology Innovation Project of CCTEG (No. 2024-TD-ZD016-01, 2024-TD-MS017). (Co-corresponding author: Fulin Tang and Ning An)

Xiaohui Jiang and Haijiang Zhu are with the College of Information and Technology, Beijing University of Chemical Technology, Beijing 100029, China. (e-mail: 2023200772@buct.edu.cn, zhuhj@mail.buct.edu.cn)

Chadei Li and Fulin Tang are with the School of Artificial Intelligence, University of Chinese Academy of Sciences, Beijing 100190, China. (e-mail: lichade2021@ia.ac.cn, fulin.tang@nlpr.ia.ac.cn)

Ning An is with the Research Institute of Mine Artificial Intelligence, China Coal Research Institute, Beijing 100013, China. (e-mail: ning.an@ccteg-bigdata.com)

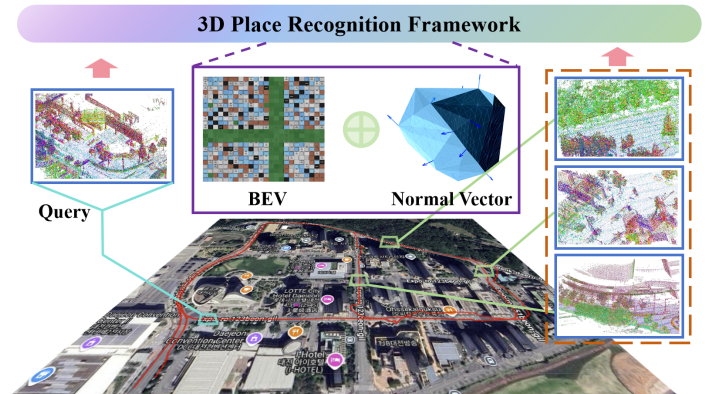


Fig. 1. Our 3D place recognition pipeline, unlike other methods, first converts the submaps into implicit neural point representations. The colored dots in the graph represent these neural representation points. Subsequently, utilizing the advantages of implicit representations, we fuse information from two modalities, namely BEV features and surface normal information of 3D segments, to generate descriptors for each submap.

Detection and Ranging (LiDAR) can obtain accurate measurement results even under various lighting conditions, such as in darkness or when disturbed by strong light. As a result, LiDAR plays a crucial role in unmanned systems. Meanwhile, with the rapid development of robotic and autonomous driving systems, there is an increasing demand for LiDAR-based place recognition [9]–[12].

Despite the rapid development of place recognition methods based on LiDAR point clouds in recent years, these methods still face the following challenges:

- In an urban environment, the LiDAR point clouds collected at the same location often exhibit inconsistencies in density and coverage due to the variability in the trajectories and motion speeds of vehicles or robots. Therefore, the algorithm must possess variability robust rotational and translational invariance, as well as invariance to point cloud density [13], [14].
- Dynamic objects within the scene, such as cars, pedestrians, and cyclists, continuously alter the 3D structure and distribution of the environment. Their presence is unavoidable and challenges the robustness of LiDAR point cloud-based place recognition [15], [16].

Most existing methods for hand-crafted feature-extraction-based 3D place recognition operate in two primary strategies. One approach is to extract features (such as local [17], [18] or global features [19], [20]) directly from the original 3D point cloud. The other approach involves first converting the raw point cloud into a structured representation (for example,

using Bird’s Eye View (BEV) [21], polar coordinate projection [22], intensity images [23], or sparse voxel grids [24]) and then extracting features.

However, existing 3D-based hand-crafted feature extraction methods generally suffer from a fundamental limitation: their reliance on relatively simplistic scene representations. These methods typically focus on feature extraction from single-modal scene representations—either directly from raw point cloud data or by converting point clouds into a specific structured representation (such as BEV or polar coordinates) and relying on it. This dependence on single representations inevitably leads to incompleteness of scene information. The reason is that while raw point clouds preserve precise 3D geometric details, they are susceptible to density variations and lack inherent rotational and translational invariance; structured representations (e.g., BEV), although providing compact global perspectives conducive to performing feature extraction, often sacrifice fine-resolution local geometry or vertical-direction information. Consequently, it is difficult to use features extracted from any single representation to comprehensively and robustly characterize complex 3D scenes, thereby constraining the upper limit of performance for subsequent 3D place recognition tasks.

To address these issues, we have deviated from the previous explicit 3D point cloud input and introduced a point-based implicit representation as the input data. We introduce this representation for three reasons:

- The point-based implicit representation is compact, flexible, and continuous. It possesses rotational and translational invariance, as well as spatial density invariance.
- This representation can efficiently provide high-quality, globally consistent surface normals, offering the opportunity to derive more discriminative place recognition descriptors.
- This representation enables more flexible online removal of dynamic objects, leading to more robust place recognition.

This paper proposes a brand-new place recognition method based on LiDAR point clouds, as illustrated in Fig. 1. This method uses a point-based implicit representation as the input for scene representation and utilizes the Signed Distance Function (SDF) and stability prediction values to filter out online dynamic objects. Subsequently, it integrates normal and BEV information to enhance place recognition capability. Specifically, we construct a normal-based descriptor by leveraging the angular differences between the surface normals of the key 3D segment. Meanwhile, we generate evenly distributed occupancy grid information using the point-based implicit representation and compute BEV descriptors. Finally, we combine these two types of descriptors to form the final descriptor.

In summary, the contributions of this article are as follows:

- We introduce a point-based implicit representation. Leveraging its consistent properties and high-quality surface normals, we construct a novel point cloud-based place recognition scheme.

- We propose a cross-modal geometric hierarchy fusion method that synthesizes structural normal descriptors with rotation-invariant BEV features, enabling resilient 3D place recognition through complementary geometric representations.
- We propose a training-free, handcrafted feature extraction method. Our implicit representation enables substantial storage savings and real-time operation. Extensive experiments demonstrate that our method outperforms state-of-the-art approaches.

II. RELATED WORKS

In this section, we will provide a comprehensive review of implicit map representation, as well as 3D point cloud place recognition methods based on handcrafted and deep learning.

A. Implicit Neural Map Representation

In recent decades, maps based on explicit representation have been widely applied in unmanned systems [25], [26]. Common methods for explicitly representing scenes include point clouds [27], triangular meshes [28], voxel grids [29], occupancy grids [30], and so on. Recently, the effectiveness of implicit neural representation has been demonstrated in the modeling of radiation fields [31] and geometric fields [32], [33]. Such a representation has facilitated many application scenarios, such as 3D reconstruction, scene generation, novel view synthesis, and so on. Based on NeRF (Neural Radiance Field) [31], DeepSDF [32], and occupancy networks [33], a large amount of research work has been carried out. However, all these works use only a single multi-layer perceptron (MLP) to represent the entire scene. Although this approach is effective, it may face poor scalability, long computation time, and high memory consumption when dealing with complex scenes. Therefore, recent approaches have adopted the hybrid representation to address the above-mentioned issues. This approach jointly optimizes the explicitly stored local latent features and the shallow multi-layer perceptron [34]–[36].

With remarkable progress achieved in efficient training methods for implicit neural representations, it has become possible to scale them up to larger scenarios, and they have been widely applied in mapping and Simultaneous Localization and Mapping (SLAM). In the mapping and SLAM systems based on RGB-D data streams, researchers have mainly proposed two types of methods. One is based on a single MLP [37], [38], and the other is based on grid-based local latent features and shallow MLPs [39]–[41] to model the geometry or radiance field of the scene while tracking the camera’s pose.

Some work has also been done for the cases where LiDAR is used as the input data stream. IR-MCL [42] and LocNDF [43] proposed a method to construct an implicit neural distance map through laser scanning and to localize the robot within this map. SHINE-mapping [44] aims to extend the implicit neural representation to large-scale outdoor LiDAR data. It stores local features in a sparse voxel format based on an octree, enabling it to handle large-scale scene data while maintaining efficient storage. In the application of SLAM, LONER

[45] integrates incremental neural mapping with an ICP-based LiDAR odometry front-end. This approach combines the modeling capabilities of neural networks with traditional point cloud registration algorithms to enhance the accuracy and efficiency of map construction and localization. NeRF-LOAM [46] proposes an implicit neural LiDAR odometry and mapping system based on an online optimizable octree-based feature grid. This method utilizes the concept of NeRF and improves the quality of map construction and the accuracy of localization by optimizing the feature grid. Compared with the previous systems, PIN-SLAM [47] has achieved greater improvements in real-time performance and map storage efficiency. It represents the scene using elastic neural points with fast indexing based on a hash table, enabling the system to operate at a speed close to real-time and saving storage overhead. Inspired by the above work, our work employs a point-based implicit representation. From this representation, we obtain the scene normal vector and occupancy information, which are the foundation for subsequent place recognition.

B. Handcrafted Methods

Early studies mainly described point clouds by extracting their geometric local features, including distance [48], point normal [49], angle [50], density [51], and so on. These methods have achieved success in point cloud registration and shape recognition. With the in-depth development of the research, researchers have started to attempt to encode the entire point cloud into a global feature descriptor. Z-Projection [52] projects the point cloud onto a certain direction (such as the Z-axis), extracts angular and height information, and then calculates the similarity through the Sørensen distance or the Wasserstein distance. Fast Histogram [53] uses a fast histogram to statistically analyze angular and height information and evaluates the similarity through the Wasserstein distance. M2DP [54] projects the point cloud onto multiple two-dimensional planes, calculates the point density on each plane, and forms a signature vector. This method avoids the calculation of point normals, improving the computational efficiency, but some information may be lost. Scan Context [55], [56] divides the horizontal space into multiple annular regions and fan-shaped regions, forming a two-dimensional height matrix. By performing nearest neighbor search through the annular key and the similarity score, good results have been achieved. To further enhance the performance, researchers have started to combine other types of features, such as intensity [57], spatial binary patterns [58], and so on. LiDAR Iris [59] converts point cloud data into "iris images", generates binary signatures through the LoG-Gabor filter and threshold operations, and then calculates the similarity through the Hamming distance. STD [18] proposes a stable triangle descriptor based on the invariance of the triangle shape. By extracting key points and encoding them into triangle descriptors, it enables efficient position matching and geometric verification. Most of the handcrafted methods are relatively natural. However, they generally encounter some problems when faced with large rotations and translations.

C. Learning-based Methods

PointNetVLAD [17] is a deep learning-based method that combines two crucial components: PointNet [60] and NetVLAD [61]. PointNet is a network that extracts features from point clouds, while NetVLAD is an aggregator that aggregates local features into a 512-dimensional global descriptor. This method lays the foundation for subsequent approaches. Based on PointNetVLAD, two methods, namely SOE-Net [62] and PCAN [63], introduce attention mechanisms. The attention mechanisms can dynamically emphasize the more important parts in the point cloud, thereby enhancing the robustness of the descriptors. Locus [64] enhances the descriptors by introducing temporal information, which can improve the robustness against viewpoint changes. HiTPR [65] partitions the point cloud into dense voxels and utilizes a transformer network [66] to enhance the correlation of local neighbors and the dependence on global context. Consequently, this method demonstrates outstanding performance in highly complex and cluttered environments. Kim et al. [67] proposed a classifier based on Convolutional Neural Network (CNN) for long-term place recognition. This approach can handle significant scene changes over a long time. Semantic Scan Context [68] addresses the translation problem by introducing semantic information. LPD-Net [69] and vLPD-Net [70] utilize Graph Neural Network (GNN) for feature aggregation, thereby effectively capturing the geometric and shape characteristics of the point cloud. DAH-Net [71] proposes a density-driven adaptive hybrid network based on the density changes of point clouds. Through a dynamic local feature aggregation and a contrastive enhanced linear attention module, it attempts to address the challenges posed by the density variations of point clouds in large-scale scenes. These aforementioned learning-based methods often suffer from relatively long training times and require substantial computational resources. Moreover, they exhibit poor performance when faced with scenarios that are not part of their training samples.

III. METHOD

This section will introduce our proposed method for Lidar-based place recognition. In Section III-A, an overview of our method will be presented. Section III-B will demonstrate the neural implicit representation. Section III-D and Section III-E will describe how we obtain descriptors with normal and BEV image information.

A. Overview

The main process of our proposed method is illustrated in Fig. 2. To better handle the random noise caused by variations in point cloud density and dynamic objects and obtain more discriminative descriptors, we use elastic implicit 3D points to represent the scene.

Considering that the LiDAR point clouds in different scanning modes need to be processed, the input of our method is several frames of point clouds $\{\mathbf{P}_1, \dots, \mathbf{P}_n\}$. The value of n is determined by calculating the distance traveled by the robot τ_n .

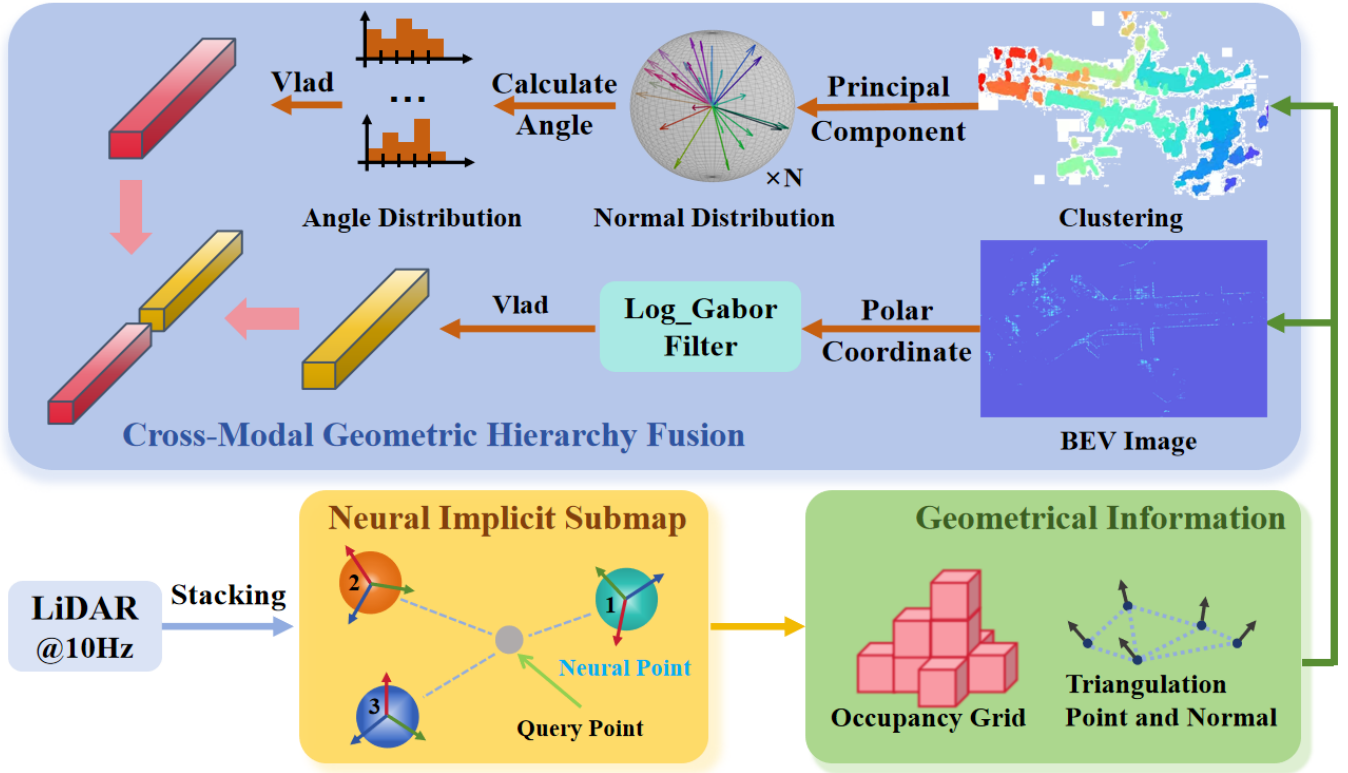


Fig. 2. Here is the pipeline of our 3D Place Recognition. A specific number of LiDAR frames are fed into form a sub-map, which is then transformed into an implicit neural point representation. High-quality occupancy grid information, triangular points, and normal vector information are subsequently derived from this representation. BEV and primary 3D segments are then obtained. The log-Gabor filter is employed to generate descriptors for the BEV. At the same time, the angular difference distribution of normal vectors is utilized to obtain geometric information descriptors for 3D segments. Finally, these two types of descriptors are fused to create a descriptor for 3D place recognition.

Subsequently, for the input point cloud sequence, we use a point-based implicit representation to encode scene geometry. Starting from the first frame, the system generates samples and labels to optimize the neural implicit map, yielding a sub-map representation. From this implicit sub-map, we extract: the scene’s occupancy grid, sample points (mesh vertices) and surface normals at these points.

Next, we remove the road surface from the mesh vertices and apply Euclidean clustering to the remaining area. For each cluster, we design a feature extractor based on angular distributions between adjacent normals, deriving multiple descriptors. Following clustering of these descriptors, we obtain the geometric descriptor $\mathbf{F}^G \in \mathbb{R}^a$. Concurrently, we project the occupancy grid into a BEV, transform it to polar coordinates, and compute local responses via Log-Gabor filtering. Keypoints are selected by maximum response, with their descriptors forming the BEV descriptor $\mathbf{F}^B \in \mathbb{R}^b$. Finally, we concatenate both descriptors into the fused representation $\mathbf{F}^{\text{fuse}} \in \mathbb{R}^{a+b}$.

B. Implicit Submap Representation With Elastic Neural Points

We will employ a memory-efficient implicit neural representation to store the geometry of the sub-map. Based on elastic neural points, this representation possesses local rotational and translational invariance. Additionally, it is unaffected by the density of the original input point cloud, has a uniform

distribution, and can remove interference from certain dynamic objects.

- 1) *Elastic Implicit Neural Point Cloud*: The results of the sub-map composed of neural implicit points \mathcal{M} are shown as follows:

$$\mathcal{M} = \{\mathbf{m}_i = (\mathbf{p}_i, \mathbf{q}_i, \mathbf{f}_i, t_i^c, t_i^u, \mu_i) \mid i = 1, \dots, N\} \quad (1)$$

Let $\mathbf{p}_i \in \mathbb{R}^3$ and the quaternion $\mathbf{q}_i \in \mathbb{R}^4$ represent the position and orientation of each neural point \mathbf{m}_i within the global coordinate frame, respectively. The optimizable latent feature encoding $\mathbf{f}_i \in \mathbb{R}^F$ of each neural point serves to capture its local geometric characteristics. To efficiently track the state of every neural point, each \mathbf{m}_i retains a creation timestamp t_i^c , a last update timestamp t_i^u , and a stability metric μ_i .

- 2) *SDF Decoder*: The joint feature coordinate encoding for scene representation is employed to achieve fast convergence and reconstruct surface holes. To ensure invariance of the prediction to the local translation and rotation of neural points, the query position is transformed from the global frame to the local frame of each neural point. Specifically, let $\mathbf{d}_j \in \mathbb{R}^3$ denote the query position in the local frame of neural point \mathbf{m}_j . This local coordinate \mathbf{d}_j is obtained by transforming the global coordinates \mathbf{p}_s of the query position using the pose of neural point \mathbf{m}_j , as

follows:

$$\mathbf{d}_j = \mathbf{q}_j(\mathbf{p}_s - \mathbf{p}_j)\mathbf{q}_j^{-1}, j = 1, \dots, K \quad (2)$$

At the query position, \mathbf{p}_s , \mathbf{K} nearby neural points are retrieved from the neural point map. For each neural point \mathbf{m}_j in the \mathbf{K} -neighborhood \mathcal{N}_P , the coordinate is computed using the above Eq 2, and then the weight ω_j of each neural point is defined as:

$$\omega_j = \frac{\|\mathbf{d}_j\|^{-1}}{\sum_{k \in \mathcal{N}_P} \|\mathbf{d}_k\|^{-1}} = \frac{\|\mathbf{p}_s - \mathbf{p}_j\|^{-1}}{\sum_{k \in \mathcal{N}_P} \|\mathbf{p}_s - \mathbf{p}_k\|^{-1}} \quad (3)$$

Subsequently, the coordinate encoding $\mathbf{g}_i \in R^C$ or each neural point \mathbf{m}_j is defined as $\mathbf{g}_i = \gamma(\mathbf{d}_j)$, where $\gamma(\cdot)$ represents the positional encoding function. The feature encoding $\mathbf{f}_i \in R^F$ and coordinate encoding $\mathbf{g} \in R^C$ of the query point are derived by fusing the encodings of the nearest neighboring points along with their corresponding weights:

$$\mathbf{f} = \sum_{j \in \mathcal{N}_P} \omega_j \mathbf{f}_j, \mathbf{g} = \sum_{j \in \mathcal{N}_P} \omega_j \mathbf{g}_j \quad (4)$$

Finally, the neural decoder D_θ generates the SDF prediction s or the query position based on these encodings:

$$s = D_\theta(\mathbf{f}, \mathbf{g}) \quad (5)$$

We employ a dynamic point filtering method based on the stability μ_i and SDF values of neural points. When updating the submap, a point is classified as a dynamic point and filtered out if its SDF value exceeds a dynamic distance threshold γ_d and its stability value exceeds a stability threshold γ_μ . Specifically, a sampled point \mathbf{p}_W in the world coordinate system is considered dynamic if it satisfies the condition $\mathbf{S}(\mathbf{p}_W) > \gamma_d$ and $\mathbf{H}(\mathbf{p}_W) > \gamma_\mu$, where $\mathbf{S}(\mathbf{p}_W)$ represents the SDF value indicating the distance from the point to the nearest surface, and $\mathbf{H}(\mathbf{p}_W)$ represents the stability value quantifying the point's consistency across multiple observations. This method effectively removes dynamic objects from the map, enhancing its accuracy and consistency.

C. Normal Vector Descriptor

After obtaining the implicit representation of the submaps, we extract the scene's occupancy information, the mesh vertices, and their corresponding normal vectors.

The process begins by discretizing the submap into a voxel grid with a predefined resolution r . At each voxel corner point within this grid, we query the Signed Distance Function (SDF) value according to the method described previously. Using these SDF values, we apply an enhanced Marching Cubes (MC) algorithm to reconstruct a triangular mesh. The MC algorithm generates vertices uniformly distributed on the reconstructed surface. The normal vector is then calculated for each vertex, defining the local surface orientation. Next, we filter the vertices to remove isolated outliers. This step refines the mesh by retaining only significant vertices along with their normals. Finally, occupancy information is derived by analyzing the SDF values at the corners of each voxel. Voxels exhibiting a sign change in their corner SDF values

are classified as occupied. This occupancy classification is essential for distinguishing between occupied and free space in the environment.

We use the GPF [72] algorithm to filter out the road surface points from the input mesh vertices. This is because the road surface points contain little geometric information and provide little benefit for extracting feature descriptors for place recognition. Subsequently, inspired by the work of FEC [73], we apply a fast clustering method for mesh vertices. This method takes the mesh vertices from which the ground points have been removed as input, and the algorithm is as follows:

Algorithm 1 Fast triangular Point Cloud Clustering

Require: mesh vertices point cloud \mathbf{cloud} , minimum cluster size min_size , distance tolerance tol

Ensure: Cluster labels for each point

```

1: Build KD-tree  $\mathbf{T}$  from  $\mathbf{cloud}$ 
2:  $n \leftarrow |\mathbf{cloud}|$ 
3: if  $n < min\_size$  then
4:   throw "Point cloud too small"
5: end if
6: Initialize  $labels[0..n-1] \leftarrow 0$ 
7:  $current\_label \leftarrow 1$ 
8: for each point  $p_i \in \mathbf{cloud}$  do
9:   if  $labels[i] \neq 0$  then
10:    continue
11:   end if
12:    $neighbors \leftarrow \mathbf{T}.radius\_search(p_i, tol)$ 
13:   if  $neighbors$  is empty then
14:     continue
15:   end if
16:    $min\_tag \leftarrow \infty$ 
17:   for each  $j \in neighbors$  do
18:     if  $labels[j] > 0$  then
19:        $min\_tag \leftarrow \min(min\_tag, labels[j])$ 
20:     end if
21:   end for
22:   if  $min\_tag = \infty$  then
23:      $min\_tag \leftarrow current\_label$ 
24:      $current\_label \leftarrow current\_label + 1$ 
25:   end if
26:   for each  $j \in neighbors$  do
27:     if  $labels[j] > min\_tag$  then
28:       Relabel all points with  $labels[k] = labels[j]$ 
29:       to  $min\_tag$ 
30:     end if
31:      $labels[j] \leftarrow min\_tag$ 
32:   end for

```

Following the derivation of clusters $\mathcal{C} = \{\mathbf{C}_1, \dots, \mathbf{C}_M\}$, points within each cluster are normalized. This normalization reduces sensitivity to noise and improves the robustness of subsequent geometric feature extraction. Specifically, all points in a cluster are isotropically scaled to be contained within a unit sphere of radius 1.

Next, the spherical domain is partitioned into 72 sub-regions based on longitude and latitude. The sphere is first divided

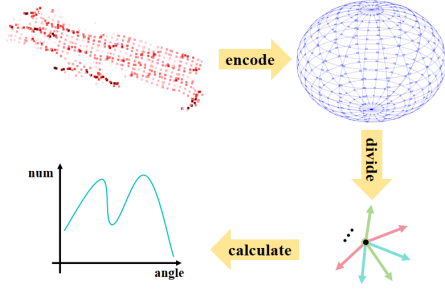


Fig. 3. The figure illustrates the extraction of geometric descriptors for 3D segments. The input is a 3D segment with surface normals; color coding indicates normal deviations. First, these normals are mapped to discrete bins on a unit sphere. Then, the average angular deviation of the normals is calculated within each bin. Finally, these per-bin statistics are assembled into the geometric descriptors.

along the z-axis into northern and southern hemispheres. By latitude, each hemisphere is further divided into two bands, resulting in 4 latitude bands globally. Longitudinal division then subdivides each latitude band into 18 sectors, formed by meridians spaced 20 degrees apart. Fig. 3 illustrates this spatial subdivision.

Following the spherical partitioning, the mean normal vector is computed for each sub-region within a cluster. The angular deviation between all unique pairs of these regional mean normal vectors within the same cluster is then calculated, generating $\binom{n}{2}$ distinct angular measurements per cluster (where n is the number of sub-regions, e.g., $n = 72$). A histogram of these angular deviations is constructed per cluster using 10-degree bin intervals (resulting in $d = 18$ dimensions), yielding a d -dimensional geometric descriptor vector $\mathbf{F}_C \in \mathbb{R}^d$ for each cluster C .

Subsequently, for each submap, the geometric descriptors \mathbf{F}_C from all its clusters are collected and normalized. The VLAD algorithm [74] is then applied to this normalized set of descriptors to generate a single submap-level geometric descriptor. To accommodate submaps with varying cluster counts (N_c), we dynamically adjust the size of the VLAD codebook (i.e., the number of cluster centers, K) during encoding, setting K proportionally to N_c . Submaps with a small N_c use a correspondingly smaller K , while those with a large N_c use a larger K . The resulting VLAD vector is then zero-padded to achieve a fixed dimensionality a . Finally, this yields the standardized geometric descriptor $\mathbf{F}^G \in \mathbb{R}^a$ for the submap. The entire process is illustrated in Fig. 3.

D. BEV descriptor

1) *Log-Gabor filters*: We project the acquired occupancy grid information onto the z-plane to obtain a BEV. The size of each pixel in the BEV corresponds to the physical size of the occupancy grids. Subsequently, we normalize the pixel values of the input image to the range $[0, 255]$ to ensure numerical stability in subsequent processing. Then, we convert the input image's coordinates (u,v) into polar

coordinate representation (ρ, θ) . Subsequently, we construct a Log-Gabor filter [75], defined as follows:

$$L(f, \omega, s, o) = \exp\left(-\frac{(\log(f/f_s))^2}{2(\log(\sigma_f/f_s))^2} - \frac{(\omega - \omega_0)^2}{2\sigma_\omega^2}\right) \quad (6)$$

Among them, f_s and ω_0 are the center frequency and direction of the filter, respectively. σ_f and σ_ω are the width parameters of the filter. Calculate each pixel point's filter responses at different scales and directions using the Log-Gabor filter. First, we perform the convolution operation, which involves convolving the filter with the input image:

$$A(\rho, \theta, s, o) = \|B(\rho, \theta) * L(\rho, \theta, s, o)\|^2 \quad (7)$$

Subsequently, for each direction o , the responses of all scales s are aggregated:

$$A(\rho, \theta, o) = \sum_s A(\rho, \theta, s, o) \quad (8)$$

2) *Maximum Index Map (MIM)*: MIM is an orientation map that records the direction of the maximum response of each pixel in all directions [76]. That is, for each pixel (ρ, θ) , find the direction o with the maximum response:

$$MIM(\rho, \theta) = \arg \max_o A(\rho, \theta, o) \quad (9)$$

The size of the MIM is the same as that of the input image, and each pixel stores a direction index. Subsequently, the FAST corner detection algorithm is utilized on the MIM to extract key points. Subsequently, for each key point, we calculate the dominant direction around it. A MIM region of size $J \times J$ is taken around the key point, and an orientation histogram $\mathbf{h}(\mathbf{o})$ is constructed for this region to count the pixel values in each direction. Then, find the peak direction o_m of the histogram:

$$o_m = \arg \max_o \mathbf{h}(\mathbf{o}) \quad (10)$$

The main direction β is:

$$\beta = \frac{\pi o_m}{N_o} \quad (11)$$

Align the direction of the MIM region concerning the main direction to achieve rotational invariance, and rotate the MIM region by an angle of β .

$$patch_\beta(\rho, \theta) = \text{mod}(patch(\rho, \theta + \beta) - o_m, N_o) \quad (12)$$

The adjusted MIM region is partitioned into $l \times l$ sub-grids. A directional histogram is constructed for each sub-grid to count the pixel values in each direction. The histograms of all sub-grids are concatenated to form a feature vector. Finally, all the feature vectors are processed using the VLAD method to obtain the final BEV descriptor $\mathbf{F}^B \in \mathbb{R}^b$.

IV. EXPERIMENTAL RESULTS AND ANALYSES

In this section, Section IV-A describes the dataset selected by us and some experimental settings, Section IV-B introduces the evaluation metrics of the experiment, Section IV-C presents the experimental results. Section IV-D and Section IV-E show the ablation experiment and running time situation respectively.

Dataset	KITTI	KITTI-360	NCLT	MulRan
LiDAR				
	Velodyne HDL-64E	Velodyne HDL-64E	Velodyne HDL-32E	Ouster OS1-64
Field of View	360° × 26.8°	360° × 26.8°	360° × 41.3°	360° × 45°
No. of Sequences	6	4	6	9
Environment	Urban	Urban	Campus	Urban

Fig. 4. Datasets for evaluation.

A. Dataset and Experimental Settings

Below, we provide a detailed description of the dataset used in this study. Our dataset includes various types of LiDAR and different application scenarios. The configuration of the LiDAR sensors used in this dataset is shown in Fig. 4.

- 1) *KITTI Dataset* [77]: This dataset was collected at 10 Hz in an urban environment using a mechanical LiDAR (Velodyne HDL-64E) mounted on top of a vehicle. We selected six sequences (00, 02, 05, 06, 07, 08) containing loop closure points for our experiments.
- 2) *KITTI-360 Dataset* [78]: This dataset was also collected at 10 Hz in an urban scenario using a LiDAR (Velodyne HDL-64E). We selected four sequences (00, 04, 05, 06) containing loop closure points for the experiment.
- 3) *NCLT Dataset* [79]: This dataset was collected using a 32-line LiDAR (Velodyne HDL-32E) mounted on a Segway robot. It was primarily collected on the University of Michigan campus, capturing variations across the four seasons, differing lighting conditions, and dynamic objects. Based on loop closure availability, we selected four sequences for the experiment: 2012-05-26 (NCLT01), 2012-08-20 (NCLT02), 2012-09-28 (NCLT03), and 2013-04-05 (NCLT04). Additionally, sequences 2012-03-17, 2012-02-04, and 2012-08-20 were used for cross-temporal location recognition experiments.
- 4) *MulRan Dataset* [80]: This dataset contains data collected from multiple scenarios in South Korea using an Ouster OS1-64 LiDAR. We selected sequences 01 and 02 from the DCC, KAIST, and Riverside scenes for the experiment; these were labeled MulRan01 to MulRan06 respectively (e.g., DCC01=MulRan01, DCC02=MulRan02, etc.). Additionally, sequences Sejong01 to Sejong03 were used to conduct cross-temporal location recognition experiments.

Our feature extraction method is manually applied to the sub-maps derived from the accumulated point clouds. To benchmark our approach, we selected five handcrafted feature extraction methods for comparison on the evaluated datasets. These methods are: Scan Context++ [56], M2DP [54], NDT [81], BoW3D [82], and STD [18]. Among them, M2DP, NDT, BoW3D, and STD can be applied directly to the accumulated sub-maps. To ensure a fair comparison, we also applied the Scan Context++ method to the sub-maps. For this purpose, we re-projected the accumulated sub-map points onto the middle frame of the sub-map to simulate a dense "scan" captured from that pose. For BoW3D, as its

TABLE I
PARAMETERS OF OUR METHOD

Parameter	Value	Description
τ_n	25m	movement distance to form a submap
K	8	neighborhood neural point number
γ_d, γ_μ	$0.006r_{max}, 4$	dynamic filtering threshold for SDF and stability
r	0.2	voxel resolution
min_size	200	minimum number of clusters
$l \times l$	6×6	number of subgrids
J	96	local patch size

default configuration is tailored to the KITTI dataset, we only conducted experiments on KITTI and KITTI-360. Experiments involving our method and five handcrafted feature-based baseline approaches were executed on a laptop equipped with an Intel Core i7-10875H CPU @ 5.10GHz and 16GB RAM. For constructing the neural implicit representations, we used an RTX 2060 GPU for acceleration. The parameter values used in our method are listed in Table I.

B. Performance Evaluation Metrics

In this article, the conditions for establishing a loop closure are defined as follows: For a query sub-map, the average position of all its frames is computed and regarded as the position of that sub-map. If the distance between this sub-map's position and that of a previous sub-map is less than or equal to 20 meters, and the difference in their indices is greater than 50, then these two sub-maps are considered positive (loop closure) pairs. The distance threshold of 20 meters was chosen based on considerations of the urban environment layout, typical LiDAR sensor range, and overall scale. Each method outputs a candidate frame along with its similarity score and compares the score against its predefined decision threshold. If the score exceeds the threshold, the match is classified as positive; otherwise, it is classified as negative. For a match classified as positive, the actual geometric distance between the query frame and the candidate frame is computed. If this distance is less than 20 meters, it is classified as a true positive (TP); otherwise, it is classified as a false positive (FP). For a match classified as negative: If no ground truth loop closure exists for the query frame (according to the criteria above), it is classified as a true negative (TN). However, if a ground truth loop closure does exist for the query frame, it is classified as a false negative (FN).

The following is how the evaluation metrics we adopt are calculated:

- 1) *Precision-Recall Curve*: In the field of place recognition, precision is defined as the ratio of true positive results to the total number of identified matches. Recall, in contrast, represents the ratio of true positive results to the total number of actual positive instances. These concepts can be formally expressed as:

$$Precision = \frac{TP}{TP + FP} \quad (13)$$

$$Recall = \frac{TP}{TP + FN} \quad (14)$$

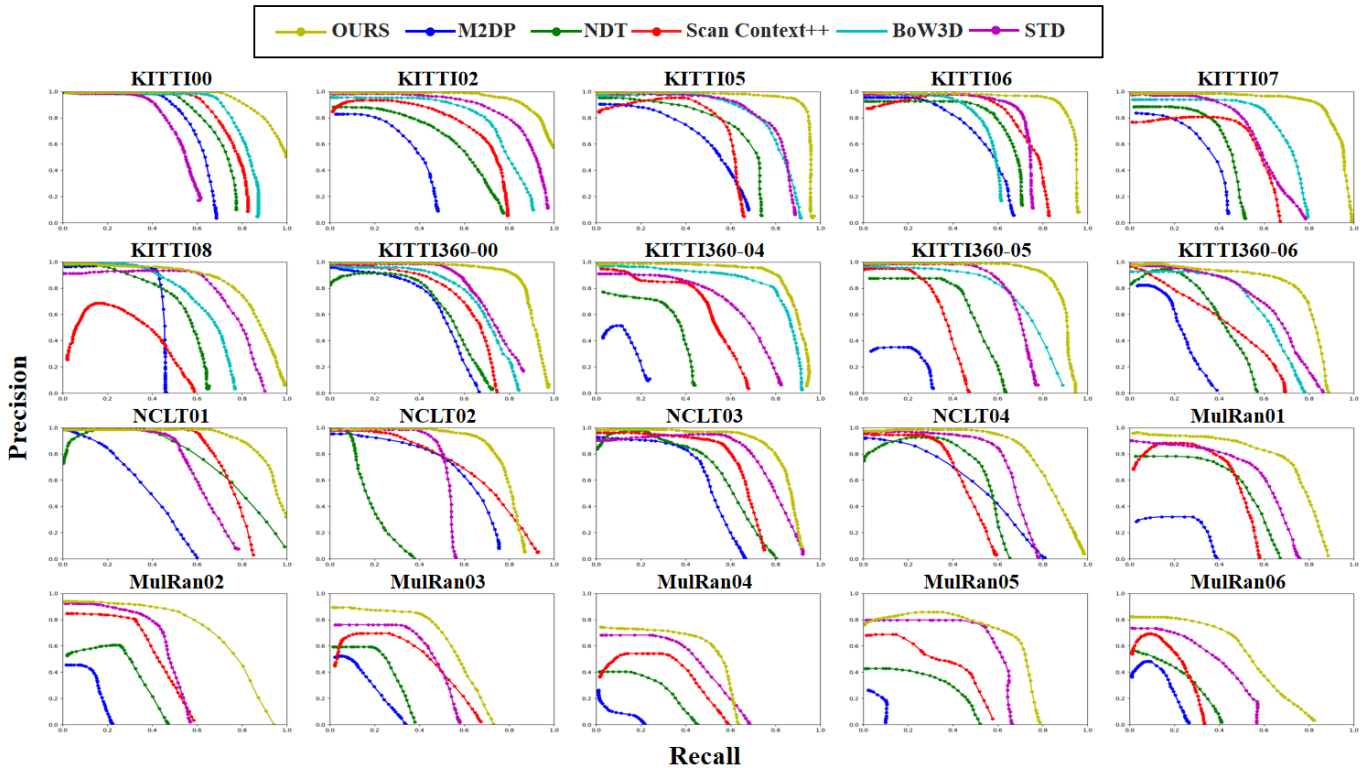


Fig. 5. Evaluation on twenty short-term sequences reveals that each subfigure illustrates the precision-recall performance of different methods. Our approach consistently outperforms all others across these sequences, demonstrating its robustness and adaptability.

Here, TP denotes the number of true positive outcomes, FP represents the number of false positive results, and FN indicates the number of false negative instances. The precision-recall curve is constructed by adjusting decision thresholds. Each point on this curve corresponds to a specific threshold setting, illustrating the precision-recall trade-off and visually demonstrating how these metrics covary with threshold adjustments.

- 2) *AUC*: The Area Under the Curve (AUC) quantifies the area beneath the Precision-Recall (PR) curve. It serves as a widely adopted metric for evaluating model performance across various decision thresholds. As a single numerical value, AUC ranges from 0 to 1. A higher AUC score indicates superior performance, reflecting the model’s enhanced capacity to accurately classify positive instances across different threshold settings.
- 3) *Max F1 Score*: The F1 score, calculated using Eq 15, represents the harmonic mean of precision and recall. This score provides a balanced measure that combines both metrics. The Maximum F1 score serves as a comprehensive performance indicator, often used to identify the optimal decision threshold. By balancing the often-competing demands of precision and recall, it effectively reconciles these priorities. The peak F1 score value indicates the algorithm’s overall best performance, demonstrating an optimal equilibrium between correctly identifying true positives and minimizing false positives.

$$F_1 = 2 \times \frac{\text{Precision} \times \text{Recall}}{\text{Precision} + \text{Recall}} \quad (15)$$

C. Experiment Performance Comparisons

To comprehensively test our method, we evaluated its performance in two major scenarios: short-term and long-term relocalization. Here, "short-term" refers to real-time detection of loop closure points, while "long-term" denotes the ability to recognize locations when revisiting the same area after a long period, specifically more than one day.

- 1) *short-term*: The PR curves for our proposed method and existing methods are shown in Fig. 5. We compared a total of 20 trajectories. Our method demonstrates superior performance compared to the existing methods. In the KITTI00 sequence, since there are only small rotational and translational changes when passing through the same location, most methods perform well. However, in scenarios with significant rotational and translational changes at the same location – such as KITTI05, KITTI08, KITTI360_04, and KITTI360_05 – existing methods tend to generate inaccuracies, whereas our method retains robust performance. When dealing with numerous similar/repetitive scenes or revisiting the same location multiple times (e.g., the six sequences in the MulRan dataset), all methods show some susceptibility to these challenging conditions. Nevertheless, our method still maintains good performance. Table II presents the AUC values and peak F1 scores. Our method surpasses the compared approaches. To provide a detailed analysis of each method, two sets of sequences for testing are presented in the figure. All methods display their optimal performance (indicated by the maximum F1 score).

TABLE II
AUC AND MAX F1 SCORES ON TESTING SEQUENCES

Method	KITTI00	KITTI02	KITTI05	KITTI06	KITTI07	KITTI08	KITTI360-00	KITTI360-04	KITTI360-05	KITTI360-06
M2DP	0.64/0.65	0.31/0.45	0.55/0.47	0.52/0.58	0.28/0.43	0.43/0.58	0.48/0.56	0.08/0.23	0.09/0.28	0.18/0.31
NDT	0.69/0.70	0.52/0.59	0.61/0.67	0.6/0.68	0.38/0.52	0.52/0.6	0.51/0.57	0.26/0.44	0.44/0.56	0.39/0.48
SC++	0.72/0.75	0.63/0.67	0.55/0.65	0.69/0.73	0.47/0.60	0.27/0.44	0.61/0.64	0.58/0.47	0.35/0.45	0.42/0.48
BoW3D	0.78/0.80	0.74/0.74	0.78/0.76	0.55/0.63	0.66/0.70	0.63/0.64	0.67/0.68	0.79/0.8	0.71/0.7	0.57/0.62
STD	0.51/0.58	0.85/0.8	0.78/0.76	0.71/0.77	0.57/0.62	0.73/0.74	0.71/0.71	0.6/0.64	0.68/0.71	0.63/0.64
Ours	0.93/0.86	0.95/0.88	0.93/0.91	0.91/0.89	0.91/0.82	0.83/0.78	0.89/0.86	0.87/0.85	0.87/0.86	0.76/0.77

Method	NCLT01	NCLT02	NCLT03	NCLT04	MulRan01	MulRan02	MulRan03	MulRan04	MulRan05	MulRan06
M2DP	0.37/0.44	0.58/0.62	0.47/0.57	0.49/0.53	0.10/0.30	0.07/0.21	0.10/0.23	0.02/0.10	0.02/0.13	0.09/0.23
NDT	0.75/0.69	0.18/0.26	0.57/0.61	0.51/0.61	0.41/0.55	0.21/0.38	0.17/0.34	0.13/0.30	0.18/0.35	0.15/0.30
SC++	0.74/0.74	0.67/0.64	0.63/0.69	0.44/0.52	0.41/0.55	0.36/0.48	0.34/0.48	0.24/0.42	0.29/0.44	0.17/0.32
STD	0.61/0.65	0.51/0.62	0.74/0.75	0.64/0.70	0.55/0.62	0.43/0.55	0.36/0.50	0.34/0.48	0.49/0.63	0.32/0.44
Ours	0.92/0.85	0.77/0.78	0.83/0.81	0.82/0.78	0.70/0.73	0.70/0.69	0.50/0.58	0.40/0.56	0.59/0.67	0.47/0.55

Note: On the left is the AUC and on the right is the max F1 score. The best-performing method is bolded.

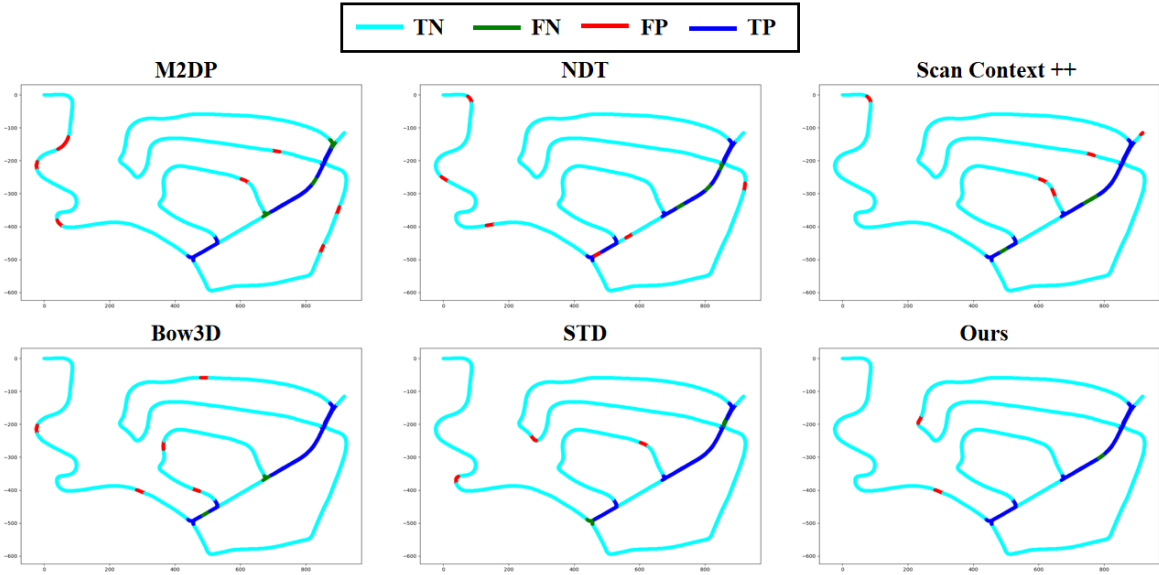


Fig. 6. Loop retrieval result using each method’s max F1 score threshold on KITTI02.

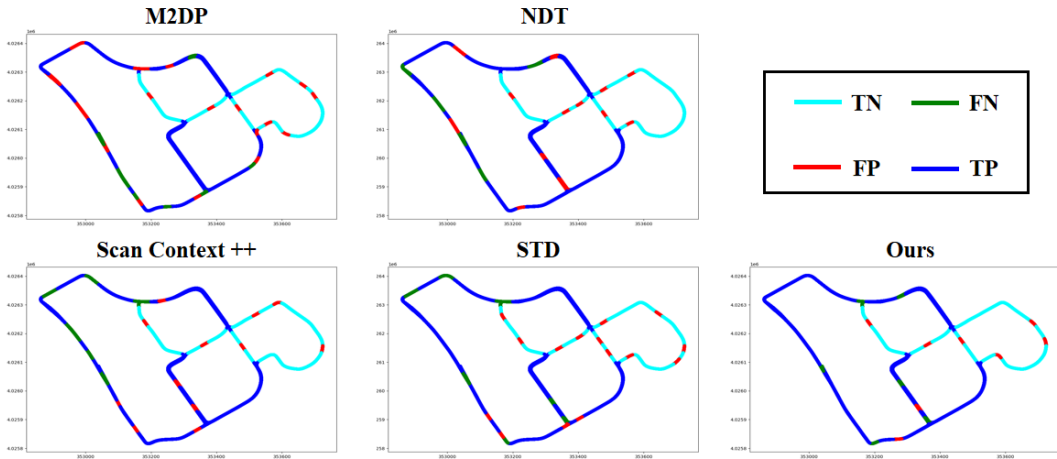


Fig. 7. Loop retrieval result using each method’s max F1 score threshold on MulRan04.

Compared to other methods, ours achieves higher True Positives (TP) and lower False Positives (FP) and False

Negatives (FN). To further highlight the distinction, we selected KITTI02 and MulRan04 tracks and visualized

TABLE III
AUC AND MAX F1 SCORES ON TESTING SEQUENCES.

Method	NCLT-L1	NCLT-L2	MulRan-L1	MulRan-L2
M2DP	0.23/0.35	0.25/0.39	0.09/0.22	0.08/0.25
NDT	0.30/0.39	0.31/0.45	0.22/0.38	0.10/0.23
SC++	0.49/0.57	0.39/0.49	0.29/0.45	0.18/0.34
STD	0.51/0.54	0.50/0.57	0.33/0.45	0.27/0.41
Ours	0.75/0.77	0.70/0.73	0.38/0.51	0.35/0.48

Note: On the left is the AUC and on the right is the max F1 score. The best-performing method is bolded. "NCLT-L1" and "NCLT-L2" represent "2012-03-17" to "2012-02-04" and "2012-08-20" to "2012-02-04", respectively. MulRan-L1", and "MulRan-L2" represent "Sejiong02" to "Sejiong01", and "Sejiong03" to "Sejiong01", respectively.

their place recognition results (including TP, FP, FN, and TN) based on each method’s optimal F1 score threshold. As illustrated in Figs. 6 and 7, it is evident that our approach generates fewer false matches and better detects loopback points, thereby delivering superior performance.

2) *long-term*: A robust place recognition system should perform reliably despite long-term environmental variations. To evaluate long-term place recognition performance, multiple intermittent datasets covering the same area were selected as the map sequence and query sequence, respectively. The results of our recall-precision experiments are shown in Fig. 8. AUC and F1 scores are presented in Table III. Our method demonstrates superior performance across all metrics. Although performance declines compared to short-term experiments on the same dataset, this results from the expanded retrieval scope and environmental changes inherent to long-term tasks, which increase place recognition complexity.

As demonstrated, our method outperforms comparative approaches. The key factors contributing to this superior performance are threefold. First, our implicit representation ensures enhanced uniformity in the acquired BEV, which directly translates to more consistent spatial descriptors. Second, our geometric descriptors strategically disregard ground-level information (prone to redundancy) while focusing exclusively on regions containing rich geometric features such as edges and corners—a distinct methodological departure. Finally, the implicit representation inherently suppresses dynamic elements, enabling effective noise interference elimination.

D. Ablation Study

To analyze the contributions of individual method components to place recognition performance, we designed ablation experiments. Specifically, we examined whether including the implicit neural representation, as well as the BEV and normal vector modules, affected 3D place recognition accuracy.

To validate the contribution of the point-based implicit representation to our place recognition framework, we conducted two experimental configurations on our dataset. The first configuration retained all default parameters, while the second removed the implicit representation module. In the absence of an implicit submap, we adopted a voxelization-based statistical method to generate occupancy grids for standard submaps. Specifically, we calculated point density

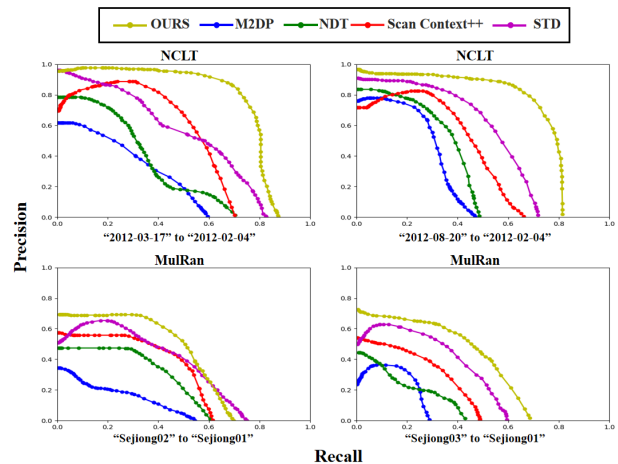


Fig. 8. Precision–recall curve NCLT, MulRan on long-term.

within each voxel and applied a density threshold matching that of implicit submaps to ensure resolution consistency. For normal vector estimation, we employed a principal component analysis (PCA)-based approach: PCA was computed on each point’s local neighborhood, with the eigenvector corresponding to the smallest eigenvalue designated as the surface normal. Ablation tests were performed across four datasets covering short-term and long-term scenarios. Quantitative results (AUC and Maximum F1-score) for all datasets are summarized in Table IV.

Building on the implicit submap representation, we conducted two additional experiments: one utilizing exclusively BEV features and the other using solely normal vector information features. Detailed quantitative comparisons are provided in Table V. As evidenced in the table, removing the implicit submap representation causes marked performance degradation. This decline stems primarily from two sources: 1) errors in surface normal estimation, and 2) inaccuracies in occupancy grid generation, both of which introduce noise that compromises 3D place recognition robustness. It can also be found that only the macro-level information from the BEV perspective and the local micro-scale information on the main 3D segments cooperate to produce a robust descriptor.

E. Computational Cost

We conducted comparative experiments on the runtime of our method to demonstrate its efficiency in 3D place recognition. We statistically analyzed the average time required to generate descriptors for each submap across all sequences, including calculating the average time for the three most critical components, and compared our method with other approaches. The running time of our method was calculated by measuring the time for descriptor generation and retrieval. The results are presented in Table V. From the table, we can see that our method is not worse than most methods in running time, even if we use implicit expressions. Our implicit representation is lightweight and efficient. We add the Voxel Hashing technique to the process of obtaining nerve points to index nerve points efficiently and reduce some

TABLE IV
AUC AND MAX F1 SCORES ON ABLATION STUDY.

Implicit Representation	BEV Image	Normal Vector	KITTI	KITTI-360	NCLT	Mulran
✓	✓	✓	0.91/0.86	0.85/0.84	0.8/0.79	0.51/0.60
			0.59/0.57	0.50/0.48	0.47/0.42	0.32/0.27
✓	✓		0.76/0.79	0.75/0.77	0.73/0.71	0.42/0.40
✓		✓	0.81/0.79	0.72/0.73	0.76/0.78	0.48/0.50

Note: On the left is the AUC and on the right is the max F1 score. The best-performing method is bolded. The individual datasets are presented as their average levels.

TABLE V
TIME CONSUMPTION (MS) OF DIFFERENT METHOD.

Method	KITTI	KITTI360	NCLT	MulRan
M2DP	73.2	74.1	80.2	76.2
NDT	465.2	451.2	387.2	392.1
SC++	62.1	59.4	57.2	63.1
STD	38.2	33.2	36.9	40.1
Ours	60.2	71.3	63.4	62.8
Ours(no implicit)	31.6	37.2	33.9	35.2
Ours(only implicit)	28.6	34.2	29.5	27.6

unnecessary optimization iterations. Meanwhile, our method for segmenting major 3D segments is also fast and efficient. Finally, real-time performance is achieved.

V. CONCLUSION

In this paper, we propose a novel 3D place recognition method inspired by implicit representations. Leveraging submap-based implicit representations, the method begins by acquiring only occupancy grids, uniform triangular points, and corresponding globally consistent normal vectors. This information is then collaboratively utilized to generate BEV images and information on clustered 3D segments, depending on exact meaning. We employ Log-Gabor filters to derive descriptors for the BEV images and compute descriptors for the 3D segments based on the angular differences between their normal vectors. By concatenating these two descriptors, we construct a cross-modal geometric hierarchy fusion feature. To the best of our knowledge, this is the first framework that utilizes implicit representations to fuse cross-modal geometric features for 3D place recognition, significantly advancing the exploitation of implicit representations’ potential in 3D place recognition. In future work, we will further explore the possibilities and roles of implicit representations in place recognition, including the development of new representation paradigms specifically tailored for this task.

REFERENCES

- [1] Du Z, Ji S, Khoshelham K. 3D LiDAR-Based Place Recognition Techniques: A Review of the Past 10 Years[J]. IEEE Transactions on Instrumentation and Measurement, 2024.
- [2] Wu Z, Wang W, Zhang J, et al. Global localization in repetitive and ambiguous environments[C]//2023 IEEE International Conference on Robotics and Automation (ICRA). IEEE, 2023: 12374-12380.
- [3] Liso L, Sandström E, Yugay V, et al. Loopy-slam: Dense neural slam with loop closures[C]//Proceedings of the IEEE/CVF Conference on Computer Vision and Pattern Recognition. 2024: 20363-20373.
- [4] Lim H, Kim B, Kim D, et al. Quatro++: Robust global registration exploiting ground segmentation for loop closing in LiDAR SLAM[J]. The International Journal of Robotics Research, 2024, 43(5): 685-715.
- [5] Liu K, Cao M. Dlc-slam: A robust lidar-slam system with learning-based denoising and loop closure[J]. IEEE/ASME Transactions on Mechatronics, 2023, 28(5): 2876-2884.
- [6] Yu S, Fu C, Gostar A K, et al.. A review on map-merging methods for typical map types in multiple-ground-robot SLAM solutions[J]. Sensors, 2020, 20(23): 6988.
- [7] Zhou B, He Y, Huang W, et al. Place recognition and navigation of outdoor mobile robots based on random Forest learning with a 3D LiDAR[J]. Journal of Intelligent and Robotic Systems, 2022, 104(4): 72.
- [8] Suomela L, Kalliola J, Edelman H, et al. Placenv: Topological navigation through place recognition[C]//2024 IEEE International Conference on Robotics and Automation (ICRA). IEEE, 2024: 5205-5213.
- [9] Gupta S, Guadagnino T, Mersch B, et al. Effectively detecting loop closures using point cloud density maps[C]//2024 IEEE International Conference on Robotics and Automation (ICRA). IEEE, 2024: 10260-10266.
- [10] Hui L, Yang H, Cheng M, et al. Pyramid point cloud transformer for large-scale place recognition[C]//Proceedings of the IEEE/CVF International Conference on Computer Vision. 2021: 6098-6107.
- [11] Vidanapathirana K, Moghadam P, Harwood B, et al. Locus: Lidar-based place recognition using spatiotemporal higher-order pooling[C]//2021 IEEE International Conference on Robotics and Automation (ICRA). IEEE, 2021: 5075-5081.
- [12] Shan T, Englot B, Duarte F, et al. Robust place recognition using an imaging lidar[C]//2021 IEEE international conference on robotics and automation (ICRA). IEEE, 2021: 5469-5475.
- [13] Jiang B, Shen S. Contour context: Abstract structural distribution for 3d lidar loop detection and metric pose estimation[C]//2023 IEEE international conference on robotics and automation (ICRA). IEEE, 2023: 8386-8392.
- [14] Zhang Z, Huang Y, Si S, et al. Osk: A novel lidar occupancy set key-based place recognition method in urban environment[J]. IEEE Transactions on Instrumentation and Measurement, 2024.
- [15] Dube R, Cramariuc A, Dugas D, et al. SegMap: Segment-based mapping and localization using data-driven descriptors[J]. The International Journal of Robotics Research, 2020, 39(2-3): 339-355.
- [16] Lai H, Yin P, Scherer S. Adafusion: Visual-lidar fusion with adaptive weights for place recognition[J]. IEEE Robotics and Automation Letters, 2022, 7(4): 12038-12045.
- [17] Uy M A, Lee G H. Pointnetvlad: Deep point cloud based retrieval for large-scale place recognition[C]//Proceedings of the IEEE conference on computer vision and pattern recognition. 2018: 4470-4479.
- [18] Yuan C, Lin J, Zou Z, et al. Std: Stable triangle descriptor for 3d place recognition[C]//2023 IEEE international conference on robotics and automation (ICRA). IEEE, 2023: 1897-1903.
- [19] Guo J, Borges P V K, Park C, et al. Local descriptor for robust place recognition using lidar intensity[J]. IEEE Robotics and Automation Letters, 2019, 4(2): 1470-1477.
- [20] Vidanapathirana K, Ramezani M, Moghadam P, et al. LoGG3D-Net: Locally guided global descriptor learning for 3D place recognition[C]//2022 International Conference on Robotics and Automation (ICRA). IEEE, 2022: 2215-2221.
- [21] Luo L, Zheng S, Li Y, et al. BEVPlace: Learning LiDAR-based place recognition using bird’s eye view images[C]//Proceedings of the IEEE/CVF International Conference on Computer Vision. 2023: 8700-8709.
- [22] Xu D, Liu J, Hyyppä J, et al. A heterogeneous 3D map-based place recognition solution using virtual LiDAR and a polar grid height coding image descriptor[J]. ISPRS Journal of Photogrammetry and Remote Sensing, 2022, 183: 1-18.
- [23] Di Giammarino L, Aloise I, Stachniss C, et al. Visual place recognition using lidar intensity information[C]//2021 IEEE/RSJ International Conference on Intelligent Robots and Systems (IROS). IEEE, 2021: 4382-4389.

- [24] Siva S, Nahman Z, Zhang H. Voxel-based representation learning for place recognition based on 3d point clouds[C]//2020 IEEE/RSJ International Conference on Intelligent Robots and Systems (IROS). IEEE, 2020: 8351-8357.
- [25] Wang S, Li H, Miao T, et al. Feature Extraction of Horizontal Plane and Optimization of 3D LiDAR SLAM in Indoor Environments[J]. IEEE Transactions on Instrumentation and Measurement, 2025.
- [26] Tang H, Niu X, Zhang T, et al. LE-VINS: A robust solid-state-LiDAR-enhanced visual-inertial navigation system for low-speed robots[J]. IEEE Transactions on Instrumentation and Measurement, 2023, 72: 1-13.
- [27] Zou Q, Sun Q, Chen L, et al. A comparative analysis of LiDAR SLAM-based indoor navigation for autonomous vehicles[J]. IEEE Transactions on Intelligent Transportation Systems, 2021, 23(7): 6907-6921.
- [28] Ruan J, Li B, Wang Y, et al. Slamesh: Real-time lidar simultaneous localization and meshing[C]//2023 IEEE International Conference on Robotics and Automation (ICRA). IEEE, 2023: 3546-3552.
- [29] Niu L, Wang Z, Lin Z, et al. Voxel-Based Navigation: A Systematic Review of Techniques, Applications, and Challenges[J]. ISPRS International Journal of Geo-Information, 2024, 13(12): 461.
- [30] Ren Y, Cai Y, Zhu F, et al. Rog-map: An efficient robocentric occupancy grid map for large-scene and high-resolution lidar-based motion planning[C]//2024 IEEE/RSJ International Conference on Intelligent Robots and Systems (IROS). IEEE, 2024: 8119-8125.
- [31] Mildenhall B, Srinivasan P P, Tancik M, et al. Nerf: Representing scenes as neural radiance fields for view synthesis[J]. Communications of the ACM, 2021, 65(1): 99-106.
- [32] Mescheder L, Oechsle M, Niemeyer M, et al. Occupancy networks: Learning 3d reconstruction in function space[C]//Proceedings of the IEEE/CVF conference on computer vision and pattern recognition. 2019: 4460-4470.
- [33] Park J J, Florence P, Straub J, et al. Deepsdf: Learning continuous signed distance functions for shape representation[C]//Proceedings of the IEEE/CVF conference on computer vision and pattern recognition. 2019: 165-174.
- [34] Xu Q, Xu Z, Philip J, et al. Point-nerf: Point-based neural radiance fields[C]//Proceedings of the IEEE/CVF conference on computer vision and pattern recognition. 2022: 5438-5448.
- [35] Müller T, Evans A, Schied C, et al. Instant neural graphics primitives with a multiresolution hash encoding[J]. ACM transactions on graphics (TOG), 2022, 41(4): 1-15.
- [36] Takikawa T, Litalien J, Yin K, et al. Neural geometric level of detail: Real-time rendering with implicit 3d shapes[C]//Proceedings of the IEEE/CVF conference on computer vision and pattern recognition. 2021: 11358-11367.
- [37] Azinović D, Martin-Brualla R, Goldman D B, et al. Neural rgb-d surface reconstruction[C]//Proceedings of the IEEE/CVF Conference on Computer Vision and Pattern Recognition. 2022: 6290-6301.
- [38] Sucar E, Liu S, Ortiz J, et al. imap: Implicit mapping and positioning in real-time[C]//Proceedings of the IEEE/CVF international conference on computer vision. 2021: 6229-6238.
- [39] Johari M M, Carta C, Fleuret F. Eslam: Efficient dense slam system based on hybrid representation of signed distance fields[C]//Proceedings of the IEEE/CVF Conference on Computer Vision and Pattern Recognition. 2023: 17408-17419.
- [40] Wang H, Wang J, Agapito L. Co-slam: Joint coordinate and sparse parametric encodings for neural real-time slam[C]//Proceedings of the IEEE/CVF Conference on Computer Vision and Pattern Recognition. 2023: 13293-13302.
- [41] Zhu Z, Peng S, Larsson V, et al. Nice-slam: Neural implicit scalable encoding for slam[C]//Proceedings of the IEEE/CVF conference on computer vision and pattern recognition. 2022: 12786-12796.
- [42] Kuang H, Chen X, Guadagnino T, et al. Ir-mcl: Implicit representation-based online global localization[J]. IEEE Robotics and Automation Letters, 2023, 8(3): 1627-1634.
- [43] Wiesmann L, Guadagnino T, Vizzo I, et al. Locndf: Neural distance field mapping for robot localization[J]. IEEE Robotics and Automation Letters, 2023, 8(8): 4999-5006.
- [44] Zhong X, Pan Y, Behley J, et al. Shine-mapping: Large-scale 3d mapping using sparse hierarchical implicit neural representations[C]//2023 IEEE International Conference on Robotics and Automation (ICRA). IEEE, 2023: 8371-8377.
- [45] Isaacson S, Kung P C, Ramanagopal M, et al. Loner: Lidar only neural representations for real-time slam[J]. IEEE Robotics and Automation Letters, 2023, 8(12): 8042-8049.
- [46] Deng J, Wu Q, Chen X, et al. Nerf-loam: Neural implicit representation for large-scale incremental lidar odometry and mapping[C]//Proceedings of the IEEE/CVF International Conference on Computer Vision. 2023: 8218-8227.
- [47] Pan Y, Zhong X, Wiesmann L, et al. PIN-SLAM: LiDAR SLAM using a point-based implicit neural representation for achieving global map consistency[J]. IEEE Transactions on Robotics, 2024.
- [48] Rusu R B, Blodow N, Marton Z C, et al. Aligning point cloud views using persistent feature histograms[C]//2008 IEEE/RSJ international conference on intelligent robots and systems. IEEE, 2008: 3384-3391.
- [49] Rusu R B, Blodow N, Beetz M. Fast point feature histograms (FPFH) for 3D registration[C]//2009 IEEE international conference on robotics and automation. IEEE, 2009: 3212-3217.
- [50] Salti S, Tombari F, Di Stefano L. SHOT: Unique signatures of histograms for surface and texture description[J]. Computer vision and image understanding, 2014, 125: 251-264.
- [51] Johnson A E, Hebert M. Using spin images for efficient object recognition in cluttered 3D scenes[J]. IEEE Transactions on pattern analysis and machine intelligence, 1999, 21(5): 433-449.
- [52] Muhammad N, Lacroix S. Loop closure detection using small-sized signatures from 3D LIDAR data[C]//2011 IEEE International Symposium on Safety, Security, and Rescue Robotics. IEEE, 2011: 333-338.
- [53] Röhling T, Mack J, Schulz D. A fast histogram-based similarity measure for detecting loop closures in 3-d lidar data[C]//2015 IEEE/RSJ international conference on intelligent robots and systems (IROS). IEEE, 2015: 736-741.
- [54] He L, Wang X, Zhang H. M2DP: A novel 3D point cloud descriptor and its application in loop closure detection[C]//2016 IEEE/RSJ International Conference on Intelligent Robots and Systems (IROS). IEEE, 2016: 231-237.
- [55] Kim G, Kim A. Scan context: Egocentric spatial descriptor for place recognition within 3d point cloud map[C]//2018 IEEE/RSJ International Conference on Intelligent Robots and Systems (IROS). IEEE, 2018: 4802-4809.
- [56] Kim G, Choi S, Kim A. Scan context++: Structural place recognition robust to rotation and lateral variations in urban environments[J]. IEEE Transactions on Robotics, 2021, 38(3): 1856-1874.
- [57] Wang H, Wang C, Xie L. Intensity scan context: Coding intensity and geometry relations for loop closure detection[C]//2020 IEEE international conference on robotics and automation (ICRA). IEEE, 2020: 2095-2101.
- [58] Ou F, Li Y, Miao Z. Place recognition of large-scale unstructured orchards with attention score maps[J]. IEEE Robotics and Automation Letters, 2023, 8(2): 958-965.
- [59] Wang Y, Sun Z, Xu C Z, et al. Lidar iris for loop-closure detection[C]//2020 IEEE/RSJ International Conference on Intelligent Robots and Systems (IROS). IEEE, 2020: 5769-5775.
- [60] Qi C R, Su H, Mo K, et al. Pointnet: Deep learning on point sets for 3d classification and segmentation[C]//Proceedings of the IEEE conference on computer vision and pattern recognition. 2017: 652-660.
- [61] Arandjelovic R, Gronat P, Torii A, et al. NetVLAD: CNN architecture for weakly supervised place recognition[C]//Proceedings of the IEEE conference on computer vision and pattern recognition. 2016: 5297-5307.
- [62] Xia Y, Xu Y, Li S, et al. SOE-Net: A self-attention and orientation encoding network for point cloud based place recognition[C]//Proceedings of the IEEE/CVF Conference on computer vision and pattern recognition. 2021: 11348-11357.
- [63] Zhang W, Xiao C. PCAN: 3D attention map learning using contextual information for point cloud based retrieval[C]//Proceedings of the IEEE/CVF conference on computer vision and pattern recognition. 2019: 12436-12445.
- [64] Vidanapathirana K, Moghadam P, Harwood B, et al. Locus: Lidar-based place recognition using spatiotemporal higher-order pooling[C]//2021 IEEE International Conference on Robotics and Automation (ICRA). IEEE, 2021: 5075-5081.
- [65] Hou Z, Yan Y, Xu C, et al. Hitpr: Hierarchical transformer for place recognition in point cloud[C]//2022 International Conference on Robotics and Automation (ICRA). IEEE, 2022: 2612-2618.
- [66] Vaswani A, Shazeer N, Parmar N, et al. Attention is all you need[J]. Advances in neural information processing systems, 2017, 30.
- [67] Kim G, Park B, Kim A. 1-day learning, 1-year localization: Long-term lidar localization using scan context image[J]. IEEE Robotics and Automation Letters, 2019, 4(2): 1948-1955.
- [68] Li L, Kong X, Zhao X, et al. SSC: Semantic scan context for large-scale place recognition[C]//2021 IEEE/RSJ International Conference on Intelligent Robots and Systems (IROS). IEEE, 2021: 2092-2099.
- [69] Liu Z, Zhou S, Suo C, et al. Lpd-net: 3d point cloud learning for large-scale place recognition and environment analysis[C]//Proceedings of the IEEE/CVF international conference on computer vision. 2019: 2831-2840.

- [70] Qiao Z, Hu H, Shi W, et al. A registration-aided domain adaptation network for 3D point cloud based place recognition[C]//2021 IEEE/RSJ International Conference on Intelligent Robots and Systems (IROS). IEEE, 2021: 1317-1322.
- [71] Wang S, Zhang Y, Zhang J, et al. Density-Driven Adaptive Hybrid Network for Large-Scale Place Recognition[J]. IEEE Transactions on Instrumentation and Measurement, 2025.
- [72] Zermas D, Izzat I, Papanikolopoulos N. Fast segmentation of 3D point clouds: A paradigm on LiDAR data for autonomous vehicle applications[C]//2017 IEEE International Conference on Robotics and Automation (ICRA). IEEE, 2017: 5067-5073.
- [73] Cao Y, Wang Y, Xue Y, et al. FEC: Fast Euclidean clustering for point cloud segmentation[J]. Drones, 2022, 6(11): 325.
- [74] Jégou H, Douze M, Schmid C, et al. Aggregating local descriptors into a compact image representation[C]//2010 IEEE computer society conference on computer vision and pattern recognition. IEEE, 2010: 3304-3311.
- [75] Fischer S, Šroubek F, Perrinet L, et al. Self-invertible 2D log-Gabor wavelets[J]. International Journal of Computer Vision, 2007, 75: 231-246.
- [76] Li J, Hu Q, Ai M. RIFT: Multi-modal image matching based on radiation-variation insensitive feature transform[J]. IEEE Transactions on Image Processing, 2019, 29: 3296-3310.
- [77] Geiger A, Lenz P, Urtasun R. Are we ready for autonomous driving? the kitti vision benchmark suite[C]//2012 IEEE conference on computer vision and pattern recognition. IEEE, 2012: 3354-3361.
- [78] Liao Y, Xie J, Geiger A. Kitti-360: A novel dataset and benchmarks for urban scene understanding in 2d and 3d[J]. IEEE Transactions on Pattern Analysis and Machine Intelligence, 2022, 45(3): 3292-3310.
- [79] Carlevaris-Bianco N, Ushani A K, Eustice R M. University of Michigan North Campus long-term vision and lidar dataset[J]. The International Journal of Robotics Research, 2016, 35(9): 1023-1035.
- [80] Kim G, Park Y S, Cho Y, et al. Mulran: Multimodal range dataset for urban place recognition[C]//2020 IEEE international conference on robotics and automation (ICRA). IEEE, 2020: 6246-6253.
- [81] Magnusson M, Andreasson H, Nüchter A, et al. Automatic appearance-based loop detection from three-dimensional laser data using the normal distributions transform[J]. Journal of Field Robotics, 2009, 26(11-12): 892-914.
- [82] Cui Y, Chen X, Zhang Y, et al. Bow3d: Bag of words for real-time loop closing in 3d lidar slam[J]. IEEE Robotics and Automation Letters, 2022, 8(5): 2828-2835.